

# Imaging and image processing in porous media research

A. Kaestner<sup>a,\*</sup>, E. Lehmann<sup>b</sup>, M. Stampanoni<sup>c</sup>

<sup>a</sup> *Institute of Terrestrial Ecosystems, Universitaetstrasse 16, CH-8092 Zurich, Switzerland*

<sup>b</sup> *Spallation Neutron Source SINQ, Paul Scherrer Institut, CH-5232 Villigen PSI, Switzerland*

<sup>c</sup> *Swiss Light Source, Paul Scherrer Institut, CH-5232 Villigen PSI, Switzerland*

Received 15 March 2007; received in revised form 26 January 2008; accepted 31 January 2008

Available online 10 March 2008

## Abstract

Three-dimensional imaging and image processing has become an important part for investigations of fluid distribution and flow in porous media. We describe two methods of computed tomography with different characteristics, namely X-ray- and neutron-based. We give an overview of image processing sequences and their methods. We investigated image enhancement with a focus on filters using partial differential equations, classification and structure identification that we used to prepare our images for quantitative evaluations. These methods are demonstrated on a partially saturated sand sample. Finally, we show an application with soil aggregates where investigations using synchrotron X-rays and thermal neutrons have led to new insights and refined fluid distribution and flow models.

© 2008 Elsevier Ltd. All rights reserved.

**Keywords:** Image enhancement; PDE filters; Image segmentation; Computed tomography; Synchrotron light; Thermal neutrons; Porous media; Soil; Water movement

## 1. Introduction

Several projects have used imaging methods and image analysis to describe and model the flow behavior in soil and more generally in porous media [1–6]. Non-destructive image acquisition such as computed tomography (CT) has the advantage over destructive imaging that the same sample can be scanned repeatedly under different initial conditions or a process can be monitored spatially and temporally. Traditionally, samples are exposed to X-rays that are sensitive to density variations in the sample. In our measurements, we combine this modality with illumination by thermal neutrons. The beam from this source type is sensitive to hydrogen atoms. By imaging modality we mean imaging systems that are based on different physical concepts and hence provide images that reveal different information. Thus, unlike many metals,

water and organic matter strongly attenuate and scatter neutrons.

Examples of applications using images are structure quantification [7–9], flow modeling [5,10], and mechanics of porous media [11,12]. The main image processing tasks are noise reduction, image enhancement, pixel classification, and pixel clustering. We review both image processing research regarding the development of processing methods and research of method applied directly in the field of porous media. The performance of some of the methods described will be demonstrated. Here, we use a three-dimensional image of a partially saturated sand sample.

We detail the useful methods in our projects and combine the results in a multi-scale and -modality context. In Sections 2–4, we describe the imaging technologies we used, the image processing, and an example that shows how the combination of neutron and X-ray-based imaging, along with image processing can lead to new insights in porous media research. The interpretation and quantification of the images requires intensive image analysis.

\* Corresponding author. Present address: Varian Medical Systems Imaging Laboratory GmbH, CH-5405 Baden-Daettwil, Switzerland.

E-mail address: [anders@kaestner.se](mailto:anders@kaestner.se) (A. Kaestner).

2. Imaging methods

2.1. Illumination by thermal neutrons

For neutron imaging, we used the Neutron Transmission Radiography (NEUTRA) facility at beam line 32 of the spallation neutron source at the Paul Scherrer Institute (PSI). NEUTRA is directly linked to the neutron source providing thermal neutrons from the moderator tank (D<sub>2</sub>O) surrounding the spallation target. Neutron radiography is ideal for quantifying water in the samples because of the atom cross-section of hydrogen. The attenuation coefficients of structural soils are an order of magnitude less than water. Imaging by thermal neutrons has been used in several investigations to quantify the amount of water contained in samples. Examples of applications using neutron radiography are observation of dynamic processes in construction materials and geological samples [13–17]. More recent detector developments also allow tomography using neutron sources. Again dynamic processes in porous media are in focus [18–20]. Hassanein et al. [20] describes a method to correct for the scatter contribution in the images. By removing the scatter component the water content can be estimated with a higher accuracy.

Digital image detection systems permit the direct quantification of water flow. In respect to sample size and spatial resolution, neutron imaging is more on the macroscopic side with the beam diameter of 40 cm and an inherent spatial resolution of about 0.1 mm. This compares to the conditions at the synchrotron radiation beam line as shown qualitatively in Fig. 1. There is an overlap in the mm-region and the reason why similar experiments were performed at both large scale facilities; the Swiss Spallation Neutron Source (SINQ) and the Swiss Light Source (SLS).

With respect to temporal resolution, the source strength of the facility plays the most important role; exposure times are shorter at higher intensity. There are a variety of imaging detection systems available, see Fig. 2. The CCD-camera system was used with a narrow box and an adapted lens system to obtain the intended field-of-view. CMOS is another semi-conductor sensor that can be used directly in the beam. The track-etch foil technique, now outdated, exposes nitrocellulose materials. The tracks from alpha-particles deliver a latent image. Temporal resolution is mainly determined by the exposure time to obtain the image. Some cases require additional readout or develop-

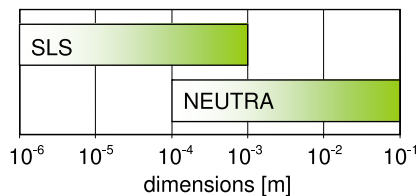


Fig. 1. Length scales for the sample size and the image resolution in synchrotron radiation imaging (SLS) and neutron imaging using thermal neutrons at NEUTRA.

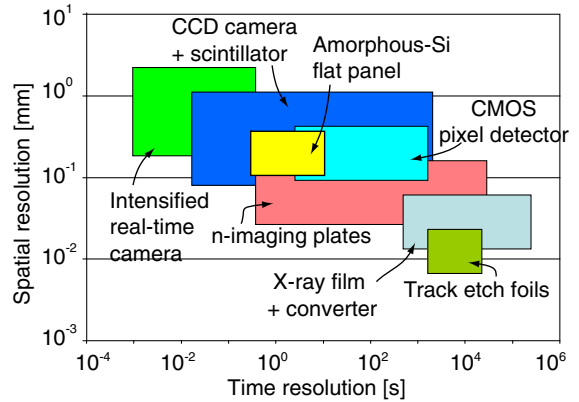


Fig. 2. Performance of neutron imaging detection systems with respect to their spatial and time resolution.

ment time. The figure is to be considered qualitative. For radiography and tomography, one has to multiply the exposure time by the number of required projections. Film and imaging plates are unsuitable for tomography. This scheme demonstrates that all improvements in temporal resolution will reduce the spatial resolution (and vice versa). However, most of the processes in soil physics like water migration are relatively slow (minutes to hours) and require only low frame rates. Therefore, the spatial resolution was of higher importance in this study. The detection system used here was a slow-scan CCD-camera with wide dynamic range (16 bit) and high sensitivity. The camera focused via a mirror on a scintillator screen. The photon emission from the scintillator has mean energy of 500 nm. This corresponds to visible green-blue light that the camera registers. This equipment is assembled sealed inside a light-impermeable box, which has to be placed perpendicular to the beam direction, Fig. 3. Using a small field of view (35 mm) to fit to the smallest sample dimensions in our experiment (5 mm diameter, 20 mm length), the inherent resolution given by the CCD pixel number (1024 × 1024) is about 0.035 mm. However, the real resolution of the imaging system is limited by the scintillator performance and light dissipation in the sensitive layer. With these limitations, resolutions 0.1 mm can be achieved with

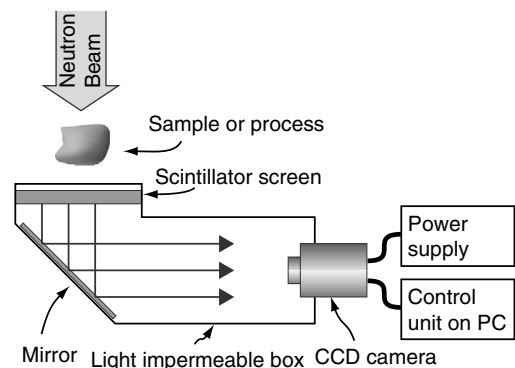


Fig. 3. Principle of the neutron imaging detection system used for the investigations, based on a cooled CCD-camera.

commercial screens. Higher resolutions can also be achieved with on-site developed screens [21]. The location of the sample holder was constant throughout the experiment. This allowed application of a pixel-wise referencing procedure, where the information in all successive images,  $I_t$ , were related to the first (dry,  $I_{t=0}$ ) one by division and normalization using the flat field,  $I_{\text{flat}}$ :

$$I_n = \frac{I_t/I_{\text{flat}}}{I_{t=0}/I_{\text{flat}(t=0)}} \quad (1)$$

The camera subtracted the dark field. This procedure fractionates the water information from the structure information of the porous medium in each pixel, thus allowing quantification of the water content.

In the tomography run, 300 projections, with exposure time of 30 s per frame, were taken over an angular range of 180°. Each projection was about 4 MB, giving the total data set for the tomography of about 1.2 GB.

## 2.2. Illumination by synchrotron-based X-rays

Synchrotron radiation X-ray tomographic microscopy (SRXTM) experiments occurred at the tomography station of the Materials Science beamline of the Swiss Light Source at the Paul Scherrer Institut in Villigen, Switzerland, see [22]. Synchrotron radiation is extracted at the straight section 4S of the SLS with a mini gap hybrid wiggler. Vertical collimation and focusing is provided by variable angle, variable curvature Rh-coated Si mirrors, which also eliminate higher order harmonics. This produces a monochromatic flux density at 10 keV of  $\approx 10^{14}$  photon/s, which can be focused onto a spot at the experimental stations with minimum size of 1 mm<sup>2</sup>. Illuminating the sample with a monochromatic beam, as opposed to the white beam illumination from conventional X-ray tubes, has the advantage of mitigating beam hardening artifacts, which negatively affect image quantification.

For our experiment, the beam energy was set to 20.0 keV to optimize absorption contrast and to provide sufficient photon flux to penetrate the large sample. After penetration of the sample, X-rays were converted into visible light by a thin Ce-doped YAG scintillator screen (Cristatec Saint-Gobain, Nemours, France). Projection images were magnified further by diffraction limited microscope optics and finally digitized by a high-resolution CCD camera (Photonic Science Ltd., East Sussex, UK). The optical magnification of the microscope was set to 4×. Considering an additional 2× eyepiece and a hardware binning of 2× (to improve the signal to noise ratio) the final theoretical pixel size was 7.0 μm, thus resulting in isotropic voxels of 7.0 μm for the reconstructed images. The field of view was 7 × 2 mm<sup>2</sup>, limited vertically by the natural vertical beam divergence and the optics acceptance. Multiple scans are necessary for samples larger than the field of view. For each measurement, between 721 and 1001 projections were acquired along with dark and periodic flat field images at an integration time of 4 s each. The dark ( $I_{\text{dark}}$ ) and flat

field ( $I_{\text{flat}}$ ) image were used to normalize the projection to represent the attenuation of the beam instead of an absolute intensity reading. The normalized images ( $I_n$ ) were computed using

$$I_n = \frac{I_0 - I_{\text{dark}}}{I_{\text{flat}} - I_{\text{dark}}} \quad (2)$$

where  $I_0$  is the acquired projection image and  $I_{\text{flat}}$  is a flat field image that is interpolated using the two flat field images that precede and succeed the current projection image.

The scanning time for one volume of interest was 70–120 min and resulted in 0.3–2.5 GB of raw projection data depending on the cropping and binning.

## 2.3. Contrast enhancing components

Quantitative analyses based on X-ray absorption are often associated with difficulties obtaining a good contrast between air, water, and solid phases. This, in turn, will complicate the classification task. To overcome this problem, one can add a contrast enhancing compound to the water. Wildenschild et al. [5] for instance added KI. Iodine has an absorption edge at 33.7 keV that enhances the contrast further than the effect of a density increase when energies near the absorption edge are used. Consequently, water could be clearly distinguished from the other two phases. In our experiments, we used CaI as tracer. We used Ca as the cationic background because bivalent cations preserve the structure of clayey soil aggregates. A concentration of 4% was selected to optimize the contrast between the three phases. A similar problem occurs in neutron-based imaging, but here the contrast can be too high. This is a technical problem since the dynamics of the detector is limited; on one hand neutrons must pass through all regions of the sample to avoid detector starvation and on the other hand the detector will be saturated if it is exposed to too many neutrons. The water is such a strong attenuator that it occasionally must be diluted with heavy water (D<sub>2</sub>O).

Adding a tracer has the drawback that density, viscosity, surface tension and contact angle between the liquid and solid phase change with the tracer concentration. This must be incorporated into models of flow behavior. Furthermore, it is important to decide how much contrast enhancer should be added. Tracer addition may increase the attenuation so much that the gray level distribution mode for the fluid phase exceeds the distribution mode of the solid phase. Alternatively, a tracer may just center the histogram mode for the fluid phase in between the two extreme modes for air and solid phase. For a non-absorbing solid phase, this decision depends only on how much the hydraulic properties are allowed to alter. However, for absorbing solid phase, like soil aggregates, it becomes a tradeoff since the attenuation will increase for the solid phase simultaneously as for the fluid. In this case the fluid mode is best placed centered between the two extreme

modes of air and solid. In addition, the salt may crystallize and block fine pores. Crystals affect the flow paths in the sample. A lower concentration is thus preferable.

### 3. Image analysis methods

Here, we give a review of some image processing and analysis methods that have been used in investigations of various sample types.

#### 3.1. Image reconstruction

Three-dimensional images are made by stacking sequences of two-dimensional slice images. The slices are tomographic reconstructions from a large number of projection images obtained by the scanning system. The inversion process required to obtain a spatial image from projections uses the filtered back-projection algorithm, see e.g. [23,24]. This algorithm consists of two steps, filtering the projection and back projecting the information on the three-dimensional image volume that represents the scanned sample. The distance from source to target is long relative to the sample size. Therefore, a parallel beam reconstruction is a valid approximation. The setups for the two imaging modalities share this property. For shorter source-to-detector distances, the cone shaped beam geometry must be considered. This is the case for desktop  $\mu$ CT scanners. The most common algorithm for cone beam CT reconstruction is the Feldkamp algorithm [25]. For the interested reader, we suggest the book by Kak and Slaney [23] that covers this topic in more detail. Ring artifact reduction improves the image quality and simplifies the segmentation work. Ring artifacts can be reduced, either in the projection/sinogram domain (pre-reconstruction) or in the image domain (post-reconstruction). In the sinogram domain, a straight line parallel to the projection angle axis represents a ring in the reconstructed image. The correction can be made directly on the sinogram by subtracting a high pass filtered average projection from the sinogram [26] or in the 2D Fourier domain using a notch filter [27]. Alternatively, the ring artifacts can be reduced in the spatial domain on the reconstructed image [28]. We used a modified approach of [26] where only artifact pixels are modified in the sinogram. This approach prevents new noise from being added to the reconstructed image.

Here, we describe several methods usually used in image processing leading to the characterization of relevant features in the original image. Fig. 4 schematically outlines the sequence of operations that are required to obtain the desired information from the image. Not all steps are always necessary and, occasionally, results from different steps are combined to provide the results. The image preparation steps, the shaded box in Fig. 4, are described in more detail in the following sections.

We also want to stress the importance of using three-dimensional operations for volume images. Choosing a

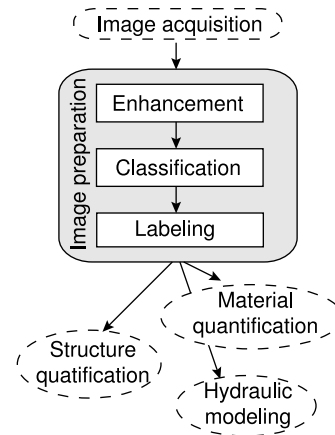


Fig. 4. Schematic of the image processing flow.

two-dimensional slice-based processing scheme will detrimentally affect the geometry of the image features. Information in the slice plane will dominate the structure. This will produce undesired shape artifacts that negatively affect the accuracy of the subsequent analyses or simulations.

#### 3.2. Image enhancement

Images are rarely perfect representations of the attenuation coefficients, since they are disturbed by optical transfer functions, scatter, and noise. Consequently, the first operation on an image is usually to apply a filter that reduces the noise level. A smoothing filter, i.e. a filter with low-pass characteristics, generally suppresses the noise. The first filters that one encounters in the image processing literature are convolution filters of different flavors, e.g. Box or Gauss filters [29,24]. Another common approach is to use a median filter that performs especially well with outliers. Both of these filters have low-pass characteristics and are spatially invariant. The effect of such filters is a smoothing that also affects sharp edged features in the image. This smoothing is undesired since it will negatively affect the resolution and the identification of edges. Noise suppression as a part of the tomographic reconstruction has the same effect.

There are solutions to the noise suppression problem that smooth regions with essentially constant intensity while maintaining or even sharpening edges. Here, we describe three different filters that all require the numerical solution of partial differential equations (PDE): the non-linear diffusion filter, the shock filter, and the inverse scale space filter. The original works by Perona and Malik [30], Catté et al. [31], and Osher and Rudin [32] use two-dimensional implementations of these filters to demonstrate the performance. The theory of these filters also supports three-dimensional implementation. Extending these filters to three dimensions is straightforward and we will show their performance on images of sand samples. Next, we outline the principles of the three filter types and apply them on two- and three-phase images of sand and soil

aggregates. For the interested reader, we suggest the book by Aubert and Kornprobst [33] which provides a deeper mathematical introduction to this class of filters.

### 3.2.1. Non-linear diffusion filter

The non-linear diffusion filter is based on the homogeneous heat diffusion equation

$$\frac{\partial u}{\partial t} = \nabla \cdot \kappa \nabla u$$

where  $u$  is the image and  $\kappa$  corresponds to thermal conductivity. The drawback of this equation is that the steady-state solution is an image with constant intensity. To overcome this drawback Catté et al. [31] modified the thermal conductivity,  $\kappa$ , into a non-linear diffusivity function controlled by the amplitude of the gradient. Following this change, the diffusivity can be small for high gradient amplitudes and near unity for low gradient amplitudes. The effect is a filter that performs smoothing in nearly homogeneous image regions, while virtually no filtering will take place near edges. The form of the diffusion filter that we use is

$$\frac{\partial u}{\partial t} = \nabla \cdot (g(|\nabla_{\sigma} u|^2) \nabla u)$$

where  $g(\cdot)$  is the non-linear diffusivity function that has a selective behavior at intensity level  $\lambda$ . The diffusivity is unity for intensities less than  $\lambda$  while it decreases rapidly for greater values. The diffusivity function is computed for  $\nabla_{\sigma} u$ , which is a gradient image smoothed by a Gaussian convolution kernel with variance  $\sigma^2$ . This regularization prevents the conservation of small irrelevant features.

The implementation of the three-dimensional diffusion filters is relatively direct thanks to the additive operator scheme (AOS) by Weickert et al. [34]. This is a numerically more stable solver for this kind of equations than a naïve implementation of a solver.

By modifying the  $\lambda$ - and  $\sigma$ -parameters of the filter, different effects can be achieved. For example the intensity of grains and pore space can be homogenized or in images where the pore space is barely resolved root structures can be enhanced while the pores are smoothed allowing a more precise segmentation of the roots [35].

Diffusion filters are implemented in the open source image segmentation and registration library ITK [36]. Sheppard et al. [37] combined diffusion filters and unsharp mask [24] edge enhancement for tomographic images of porous materials. The unsharp mask operation does however introduce overshoots near the edges. This may disturb later processing steps.

### 3.2.2. Shock filter

The second filter type is the PDE-based shock filter that was introduced by Osher and Rudin [32]. They described the filter in the form

$$\frac{\partial u}{\partial t} = -|\nabla u| \text{sign}(\Delta u)$$

here  $u$  again is the image to be enhanced and  $\Delta u = \nabla \cdot \nabla u$  denotes the Laplacian operator. This original form is sensitive to noise. Every rapid change in the image will be enhanced, including outliers originating from noise. To avoid enhancing the noise Alvarez and Mazorra [38] added a diffusion term to the original shock equation. The resulting equation is used in our three-dimensional implementation. They also smoothed the Laplacian with a Gauss filter to prevent small structures from generating shocks on their edges. The equation we use in some of our enhancement tasks is here rewritten such that it is clear that the curvature,  $H$ , is used by the diffusion term:

$$\frac{\partial u}{\partial t} = \underbrace{c|\nabla u|H}_{\text{Diffusion term}} - \underbrace{|\nabla u| \text{sign}(\Delta_{\sigma} u)}_{\text{Shock term}}$$

where the constant  $c$  controls the amount of diffusion to include in the solution. The local curvature was computed using second derivatives, Thirion and Gourdon [39]. The effect of this equation is a filter with shock effect perpendicular to the edge and diffusion parallel to the edge. The shock filter is best applied on images that have smooth edges and noise models with low spatial correlation. For images with a high spatial noise correlation, the noise regions will be enhanced as structures unless strong smoothing is applied. Welk et al. [40] give the theoretical foundation of the shock filter.

### 3.2.3. Inverse scale space filter

A different approach to define enhancement filters is presented by total variation filters, introduced by Rudin et al. [41]. These filters are based on the concept of minimizing the variation in the image using a cost function. Developments of this filter lead to the regularized inverse scale space filter (ISS-filter) that was introduced by Scherzer and Groetsch [42] who defined the filter for a linear scale space. This filter combined the diffusion filtering methods and regularized filtering methods. Burger et al. [43] extended the theories to support non-linear scale spaces and formulated a simple and well defined stopping criterion. Generally, the inverse scale space filters start with any image. During the iterations first large scaled features are added and with an increasing amount of iterations also finer features appear. The principle is based on the minimization of a functional such as

$$\min_u \left\{ \underbrace{J(u)}_{\text{Regularization}} + \lambda \underbrace{H(f, u)}_{\text{Fidelity}} \right\}$$

where  $u$  is the filtered image,  $f$  the original image, and  $\lambda$  is a regularization parameter. This functional has a minimum at the steady-state solution of the following coupled system of constrained PDEs

$$\begin{aligned} \frac{\partial u}{\partial t} &= -p(u) + \lambda q(f + v, u) \\ \frac{\partial v}{\partial t} &= \alpha q(f, u) \end{aligned} \quad (3)$$

where  $\alpha$  is a time scaling constant of the decomposed noise solution  $v$ . Filter behavior depends on the definition of the regularization function  $p(\cdot)$  and the fidelity function  $q(\cdot, \cdot)$ . We demonstrate the total variation in  $L^2$  (TV-L2) filter described by Burger et al. [43]. This filter is, as they say, a natural choice for image enhancement as it produces a sharp and clean approximation of the input image. With this filter, Eq. (3) takes the following form

$$\begin{aligned} \frac{\partial u}{\partial t} &= \nabla \cdot \left( \frac{\nabla u}{|\nabla u|} \right) + \lambda(f - u + v) \\ \frac{\partial v}{\partial t} &= \alpha(f - u) \end{aligned} \quad (4)$$

For this filter Lie and Nordbotten [44] proved that  $\alpha \leq \frac{\lambda}{4}$  must be chosen to avoid oscillating solutions. To suppress strong noise and/or large features the regularization parameter  $\lambda$  must take small values, i.e.  $\lambda \ll 1$ .

### 3.2.4. Demonstration of enhancement filters

We demonstrate the performance of the described filters using an image taken from an evaporation experiment. The sample was a cylinder filled with sand and a solution of water and  $\text{CaI}_2$  (4% by weight). The used image has the dimensions  $256 \times 256 \times 256$  voxels and a resolution of  $7 \mu\text{m}/\text{voxel}$ . Fig. 5 shows the mid slice of the original image and of the filtered images using non-linear diffusion filter,

shock filter, and ISS filter. The figures show that with the filter settings used, the diffusion and ISS filters produce the smoothest homogeneous regions. The diffusion filter produces somewhat irregular edges. This is because the edges essentially are untouched by this filter. Furthermore, the diffusion filter uses constants for the contrast- and scale-parameters. Better edge performance can be expected for the diffusion filter when a parameter update method is used. Perona and Malik [30], used a percentile of the histogram of the absolute gradient image to select  $\lambda$ . Another method to find  $\lambda$  is proposed by Black et al. [45] who used robust statistics based on the median of the gradient image.

The performance of the shock filter is not impressive for this example image. The reason for this is that the image characteristics do not correspond to the optimal conditions for this filter; smooth edges (several pixels wide) and spatially uncorrelated noise. Tuning the filter for this image was a difficult balance between smoothing the homogeneous regions and eroding relevant edge features. Fig. 6 shows the effect of a shock filter on a more relevant sample. The histograms of the original and processed images show that not only a smoothing takes place but also a sharpening that minimizes the tail distributions.

In Fig. 7, we show some edges in more detail. In this figure the shock filter is replaced by a Gauss filter to show the difference in how edges and homogeneous regions are han-

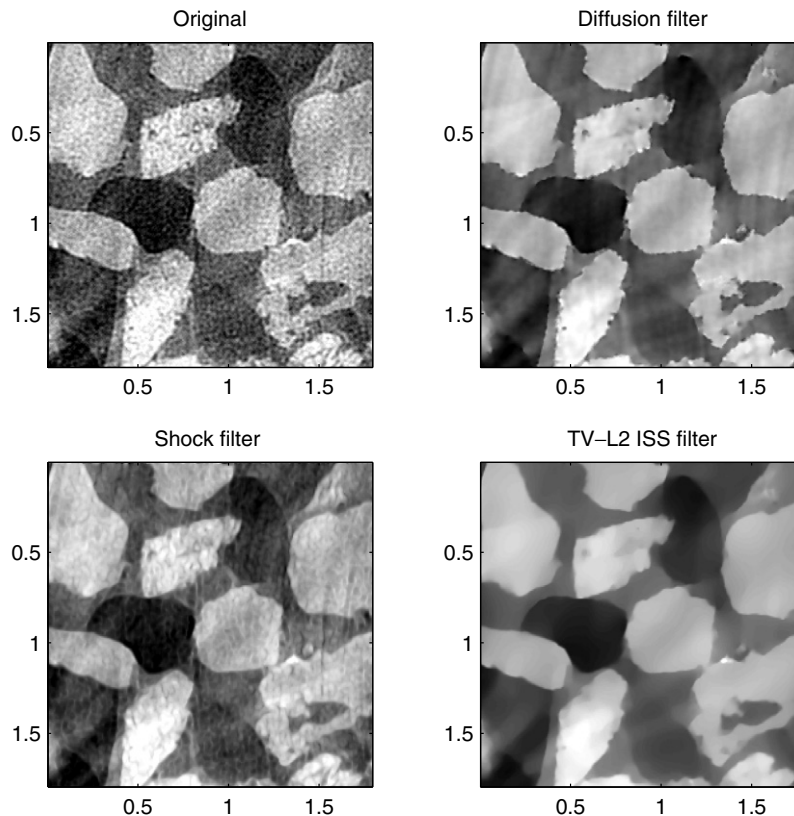


Fig. 5. Performance examples using the described filters on an X-ray image. The image shows sand grains, water, and air. All images are displayed with the same intensity window and the axis units are given in mm. Original image courtesy of P. Lehmann and D. Or, Swiss Federal Institute of Technology Lausanne, Switzerland

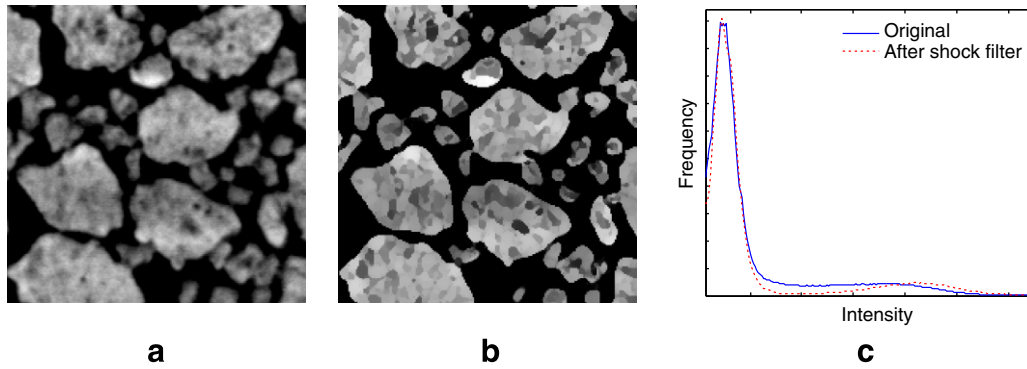


Fig. 6. An example that shows the effect of a shock filter applied on the original image (a), the resulting edge enhanced image (b), and the histograms of the two images (c). The example image is a slice extracted from a 3D image of an arrangement of soil aggregates scanned at a resolution of 125 μm/voxel using thermal neutrons. The voxel intensity represents the local water content.

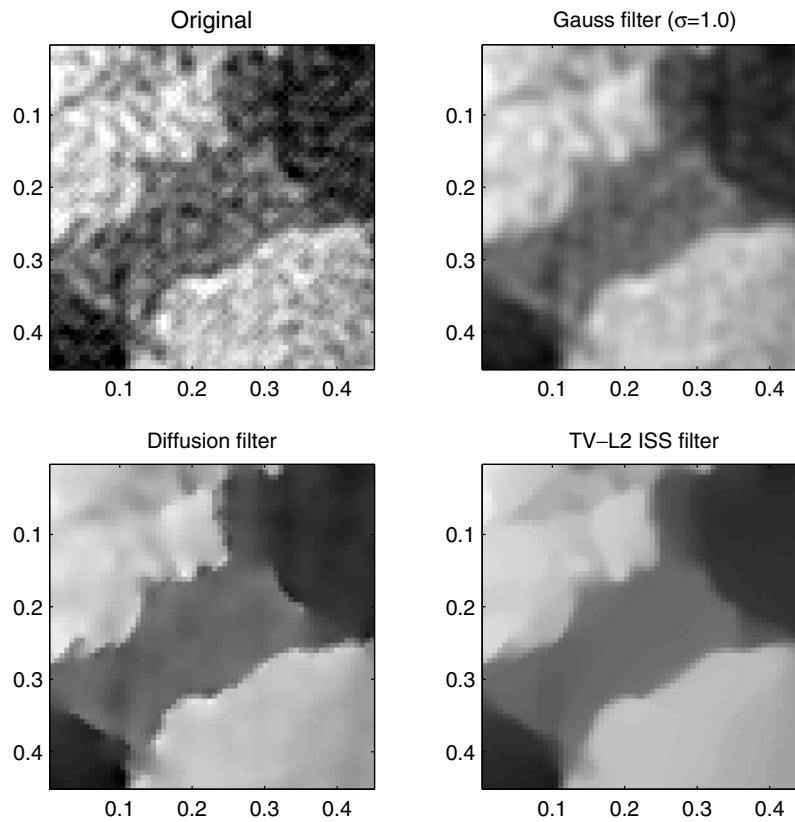


Fig. 7. A detail of the image that shows some edges in closer detail. All images are displayed with the same intensity window and the axis units are given in mm. Original image courtesy of P. Lehmann and D. Or, Swiss Federal Institute of Technology Lausanne, Switzerland.

dled by the filters. The histograms of the images in Fig. 5, show that the two PDE-based methods produce the sharpest histograms. A different way to quantify the image improvement is to compute the total variation ratio to the original image:

$$TV_r(u, v) = \frac{\sum_{\Omega} |\nabla u|}{\sum_{\Omega} |\nabla v|} \quad (5)$$

where  $\Omega$  is the set of voxels, and  $u$  and  $v$  are images. With this metric we obtain  $TV_r(u_{Gauss}, u) = 0.7190$ ,  $TV_r(u_{Diffusion}, u) = 0.2068$ , and  $TV_r(u_{ISS}, u) = 0.1654$ . A

small value indicates homogeneous regions. Combined with the histogram (Fig. 8) this information tells that the ISS filter followed by the diffusion filter cancels most noise and preserve the edges best. Still, for initial investigations smoothing by convolution or median filters are methods since they are available in most image processing tools and deliver the result faster.

### 3.2.5. Memory efficient implementation of PDE-based filters

A disadvantage of the PDE-based filters is the heavy use of computer memory. In the worst case, memory consump-

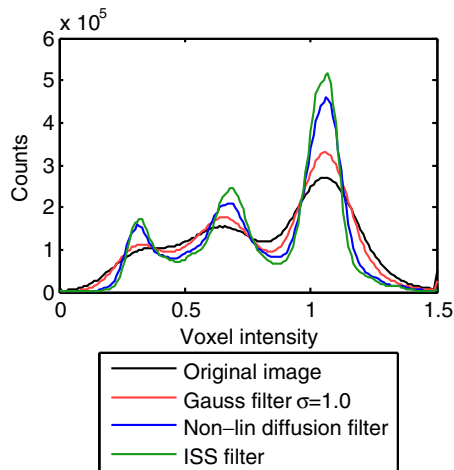


Fig. 8. Histograms of the filtered images. The histogram of the original image is added as reference.

tion can reach seven times the original image size. The solution is either to process small slabs of the image or to do a thorough redesign of the filter implementation. The latter approach resulted in a filter that only requires a small fraction of the image size for intermediate information storage.

The principle exploits the fact that PDE filters only require local information to update a pixel and that the sub-operations of the filters are separable, i.e. each direction can be filtered independently from the others using one-dimensional filter kernels. The latter is an essential feature that allows the use of 2D images for intermediate results. This saves a large amount of memory by using first-in first-out (FIFO) queue data structures to store the currently relevant image information. We used image slices in the  $XY$ -plane as the smallest image fraction to process. The items stored in the queues are pre-computed image slices, e.g. Gauss (2D) filtered slices or gradient slices in the  $X$ - and  $Y$ -directions. The third dimension is processed when the output slice is finalized. Several queues may be required to support the computations. When a queue item is no longer needed, it is removed from the queue and memory can be released. The inverse scale space filter requires that the original image is used for the fidelity term in each step. This makes the implementation less memory efficient than diffusion and shock filters.

### 3.3. Classification

The choice of a classification method is not as straightforward as the aforementioned enhancement methods. It depends on the number of classes to be identified, the separability of the classes, the size of the relevant features, etc. One method may be ideal for one application but may not work for others. In general, a good classification method should preserve the class distributions including their tail distributions as illustrated in Fig. 9. In cases of tail truncation some pixels are assigned to the wrong class. These pixels are mostly near the edges. This will detrimentally affect

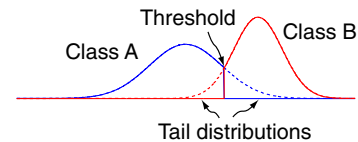


Fig. 9. Truncated and preserved tail distributions.

the accuracy of the classification of the feature for use in subsequent analysis or simulation.

The difficulty of identifying an efficient classification method is reflected by the great variety of published methods as we show in the following sections. Here, we only consider unsupervised methods since the supervised segmentation becomes impractical for most applications in porous media research; there are usually too many items to identify. Furthermore, the result of supervised methods may be biased by the arbitrary choices of the operator.

The classification task can be approached in several ways. First the task can be composed into two sub-tasks; identifying and providing information about the classes present in the image and assigning classes to the pixels. In some methods these sub-tasks are clearly separated while in others there is a continuous interaction between the two tasks.

#### 3.3.1. Histogram-based thresholding

This is a common initial approach to assign classes to the pixels in an image. The principle is based on the estimation of a global threshold level from the intensity histogram of the image. The pixel classes are assigned by comparing the intensity with this threshold value.

A classic method of this type is described by Otsu [46] who uses the criterion that the in-class variance is minimized while the between-class variance is maximized. When the noise is identified as Gaussian, an alternative method is to fit a sum of Gaussian functions on the histogram data and use the estimated parameters to determine the threshold levels using decision theory, see e.g. [47]. Metrics based on the histogram entropy also has been used to identify threshold levels [48]. To find a threshold level in mono-modal histograms Rosin [49] used a method based on the location of the histogram knee, i.e. the point where the tangent of the main histogram peak meets the tangent of the asymptotic low probability tail.

Using strict gray-level intervals, such as the ones provided by histogram-based thresholding methods, generally truncates the tail distributions and results in a number of incorrectly classified pixels. This makes these methods unsuitable as a final segmentation method. Histogram-based thresholding, however, often serves well as an initial condition for more complex methods, described in the following.

#### 3.3.2. Region growing

The concept of region growing is that small regions are grown by assigning the region class to neighboring pixels.

This growth is repeated until a termination condition is fulfilled [50]. The seed regions can be defined by pre-segmentation from a histogram-based method. Fan et al. [51] provides a recent comparative study of seeded region growing methods. Morphological methods can also be used to describe the region growing [52].

Vogel and Kretschmar [53] used region growing for the segmentation of soil samples and region growing is also the concept used by Ketcham [54] in the BLOB3D analysis package.

Refinements of the seeded region growing approach are methods that locally adapt the threshold level to the local conditions during the iteration. This type of segmentation has been used to track fine features like roots or wormholes in soil samples [55].

### 3.3.3. Iterative class property minimization

This is a class of segmentation methods that iterates over a set of pixels until a minimization criterium is fulfilled. Some methods use a pre-segmentation by a histogram-based method as initial condition. Further refinement of difficult regions like edges is handled by other methods. The presegmentation saves processing resources for the difficult regions, both in terms of processing time and memory. An example of this approach is the indicator kriging segmentation by Oh and Lindquist [56]. Al-Raoush and Willson [57] have also used this method.

An example of a method that operates on the whole image is the fuzzy C-means method [58]. It belongs to a class of methods that minimize an objective function based on a clustering criterion. This method is well suited for multi-class segmentation. Wildenschild et al. used a method based on a combination of C-means and a segmented image of the dry sample to segment images of the wet samples [59].

### 3.3.4. Pyramid-based segmentation

Pyramid-based segmentation uses the concept that the relevant features must have a specified size to be accepted in a class. This scale concept is realized by using a scale pyramid [29,58]. A scale pyramid is constructed by successively down-sampling the image to increasingly coarser scales. The sampling procedure uses Gaussian- or box-filter, this result in either a Gaussian- or a Laplacian pyramid. In its simple form, the highest (coarsest) level is segmented into two or more classes. The class information from this level is propagated down to the next level by an update scheme, which produces a segmented image at a finer scale. The segmentation process finishes when the class information has propagated down to an image of the initial scale.

In general, the pyramid provides a framework for segmentation that leaves two major decisions open; the top level segmentation, and the class propagation down the pyramid.

The top level segmentation is crucial for the outcome of the segmentation. In our three-phase segmentation we used the fuzzy C-means algorithm for the top level segmentation.

Classes can be propagated using several methods. The class of the child can be assigned by the most likely parent. This is known as parent relinking and an early application of this approach was presented by Burt [60] who iteratively refined the pyramid. A second approach is to use probability schemes. In this approach a combination of class statistics and local probability is used. In some applications even local structure information such as edges is used in the decision [58, pp. 441–448]. For a more detailed review of the development of pyramid-based methods we refer the reader to Marfil et al. [61].

To set up a pyramid, the number of levels must be determined; this is a trade-off between the smallest feature that has to be detected and the noise level in the image.

### 3.4. Structure clustering

A recurring task in our investigations is to identify single items in the images. There are various reasons for this. Some examples are: to compute the grain size distribution, selecting items with a specific shape and size, and to identify contact points between items. Most often, we apply the watershed segmentation algorithm for this task [52, pp. 267–292]. In contrast to a simple connected-component labeling procedure, this labeling method can also successfully identify items that touch each other as two individual items.

The underlying principle of the watershed segmentation is based on the analogy of a landscape that is flooded by water as shown in Fig. 10. Catchment basins are regions that share a common local minimum and will be assigned a label. The ridges of the hills will form watershed lines, i.e. region boundaries in the image. Dams will be built to prevent water from overflow into another catchment basin. These dams will also be a part of the watershed lines. The labeling procedure terminates when the whole image only contains labeled regions and watershed lines.

A successful labeling procedure involves several steps. Firstly, the watershed segmentation algorithm requires an elevation map that represents the landscape to be flooded. In our case, this elevation map is generated from a bi-level

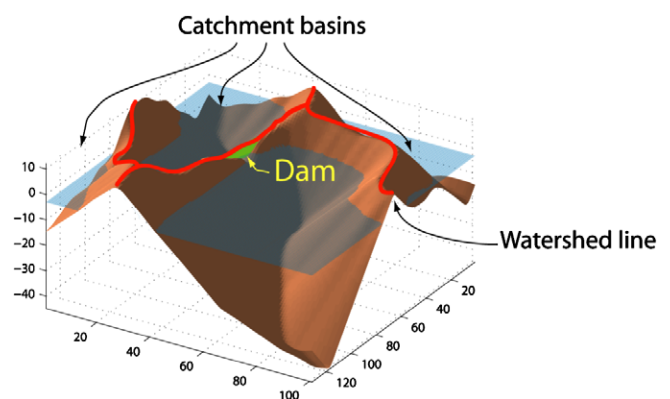


Fig. 10. The landscape model used by the watershed segmentation.

image using the Euclidean distance transform,  $D_\varepsilon(\cdot)$ . This operation transforms the background pixels of a bi-level image into a distance field. Each pixel is assigned a Euclidean distance to the nearest foreground pixel. In our experience, a good elevation map  $D_f$  of image  $f$  is represented by

$$D_f = D_\varepsilon(f) - D_\varepsilon(f^c)$$

where  $f^c$  represents the complementary image of  $f$ , e.g. the pore space of an image that represents a sand sample. This distance map requires a post-processing step using the bi-level image to mask out the items from the segmented regions. In the landscape analogy the valleys represent the items, e.g. grains, and hills represent the background (Fig. 10). Irregular shapes such as sand grains will produce several local minima for each grain in  $D_f$ . These minima lead to an over-segmentation, since each minimum will result in a catchment basin. The over-segmentation behavior can be avoided by imposing minima regions that include all local minima for each item. This procedure is described by Soille [52, pp. 279–280]. Videla et al. [62] suggests using the semi-variogram to determine the size of the particles in the samples. They used this size to define the local minima. The complete processing sequence for watershed segmenting an image is outlined in Fig. 11.

The morphological operations and transforms described here are supported by commercial image processing software packages such as Matlab and IDL as well as open source libraries like ITK. Calculation speed can be improved by implementing the algorithms for 3D image processing using C/C++. A reason for this is that the commercial code is partly based on general purpose command interpreting processing engines that rarely meet the performance level of well-tuned compiled code.

An alternative to the morphological segmentation is given by level sets and fast marching methods. An introduction to these methods is given in [33] and an overview, with more recent results and applications, is provided by Osher and Paragios [63]. In general, these methods grow regions by minimizing a cost function consisting of two terms, one that stops the evolving surface and the other controls the direction and rate of surface movement. A problem with active contour and level set methods is to find

good stopping criteria. To overcome this problem, Sheppard et al. [37] introduced a combination of active contours and watershed propagation, which gives a natural stop on the watershed lines.

#### 4. Application

In the following section, we apply the image analysis methods described above to study the hydraulic properties of soil aggregate packings. Two imaging techniques are used: neutron radiography for monitoring in real time and two dimensions the water distribution through series of soil aggregates; and X-ray tomography to image the pore geometry and the water distribution between and within soil aggregates at stationary conditions. The two techniques provide complementary information for deriving the hydraulic properties of aggregated media. To derive such properties we make use of the image analysis methods described before.

Surface soils are often structured as aggregates separated by large inter-aggregate pores. Such a structured state is crucial for the movement of water, air and solutes. The hydraulic behavior of aggregated soils is in first place characterized by the duality of the large inter-aggregate pores and the micro-pores within the aggregates. The link between the properties of the individual aggregates and those of large aggregate packings is still missing or it is based on empirical and parametric approaches. In order to find this link the following experiments have been performed.

Neutron radiography has been used to image in real time and in two dimension water infiltration through series of soil aggregates. The measurements have been performed at the NEUTRA facility of PSI, Switzerland. A detailed description of the measurements is reported in [64]. The obtained radiographs have been corrected for scattering corrections as described in Section 2.1. From the corrected radiographs and from comparison with dry aggregates, the water content distribution through the series of aggregates was calculated using Eq. (1). The water content distribution is shown in Fig. 12. The time-series of radiographs show how water moves through the soil sample and how

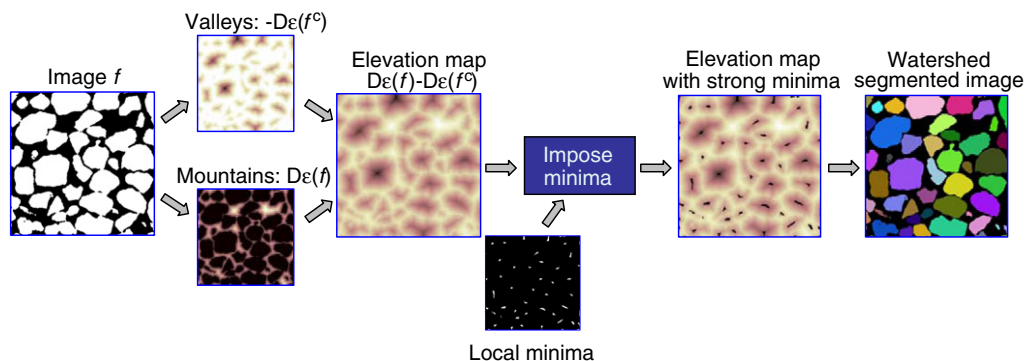


Fig. 11. Schematic illustration of the processing flow for watershed segmentation.

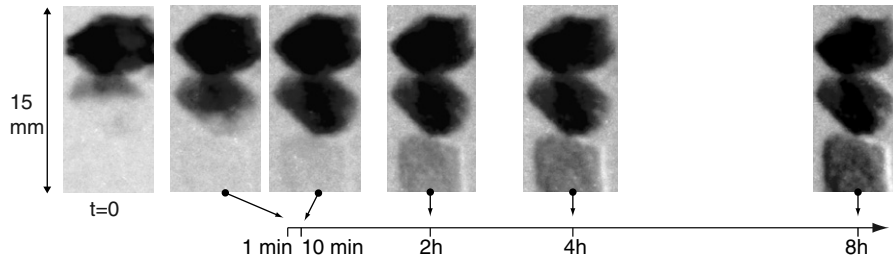


Fig. 12. A time series of images that shows the movement of a few droplets of water in an arrangement of aggregates. The sequence was captured with thermal neutrons. A dry reference image was subtracted from the images in the sequence. Dark regions have high water content.

the flow is affected by heterogeneities such as the aggregate–aggregate contacts. Water is well visible thanks to its high neutron attenuation coefficient. Neutron radiography is an optimal tool for imaging dynamic and fast process such as water infiltration in thin soil samples, where small variations in water content can be quantified with high precision. From this type of experiments, it is possible to derive macroscopic hydraulic properties such as water retention curve and hydraulic conductivity [64]. Limitations of taking time-series neutron radiography are due the two-dimensional approximation and the limited spatial resolution. Three-dimensional information can be obtained by performing neutron tomography of the samples at stationary conditions. However, pores smaller than 0.1 mm are unlikely to be visible via neutron tomography. In the case of soil aggregates, the intra-aggregate pores and possibly discontinuities at the aggregate–aggregate contacts are not detectable. Therefore, imaging techniques with higher spatial resolution are required in order to resolve the geometry of the pore space and relate it to the measured hydraulic properties.

Pore geometry and fluid distribution inside and between soil aggregates have been obtained by means of X-ray tomography. The experiment has been performed at the TOMCAT beam line of the SLS-PSI (Section 2.2). The experimental set-up allowed a field of view of  $2.5 \times 11$  mm and a resolution of  $5.92 \mu\text{m}$  (voxel side length). The sample is a cylinder containing two soil aggregates placed one on the top of the other. At the bottom of the cylinder a porous plate was connected to a water reservoir for wetting the sample at controlled water potential. In order to increase the visibility of the liquid phase we added  $\text{CaI}_2$  at a concentration of 4% by weight. The contact region between the two aggregates was tomographed at two equilibrium conditions: at a matric potential  $h = -0.025$  and  $-1.4$  m. Objective of these measurements was to evaluate the distribution of water in the contact region. The contact region was expected to have different hydraulic properties compared to the aggregate interior. The roughness of the aggregate surface likely creates irregular contacts with large pores, which become rapidly drained and which affect the conductivity of the entire medium. To evaluate and quantitatively describe this mechanism, the two aggregates, the liquid and the air phases have to be distinguished. Additionally we defined

a contact surface which separates the two aggregates. The distribution of water on this contact surface gives the flow-cross section between the aggregates and it is an expression of the hydraulic conductivity of the contacts.

In the images from the X-ray scan, the water distribution between the two aggregates is clearly visible in the segmented image (Fig. 13). X-ray imaging allows distinguishing the wet structures from water located in the voids and between the structures as opposed to neutron imaging. Fig. 13 shows the segmented three phases mapped on the identified medial surface and projected on the horizontal image plane. The three-phase segmentation was made using the previously described hierarchical classification method and top-level segmentation using a Gaussian pyramid and fuzzy C-means classifier. The were classes propagated down the pyramid using a maximum a posteriori update scheme based on class statistics from the current parent image and local class probabilities computed from the neighborhood of each parent voxel. The medial surface between the two items was identified using watershed segmentation. Two seed regions were used for this; one representing the upper aggregate and the other the lower aggregate. The seeds were created using the segmented top- and bottom-most slices. Using the distance field defined in Section 3.4 we obtained the medial surface. This surface is located on an equal distance from the two aggregates. The figure shows that the water filled contact area is much wider between wet aggregates than between dry ones. In the dry case the contact area is reduced to the small areas where the aggregates touch each other, black in the figure. In the wet case the contact area is the sum of the gray and black regions in Fig. 14.

From the water distribution on the contact surface we interpreted the hydraulic conductivity of series of aggregates. In this sense, X-ray tomography and neutron radiography provide complementary information for describing the hydraulic properties of soils. Neutron radiography can be used to image water content distributions quantitatively and with high temporal resolution. These data can be used to derive macroscopic transport properties. X-ray tomography can be used to image the three-dimensional geometry of the pores. Based on this information hydraulic properties can be derived and compared to those observed in dynamic experiments.

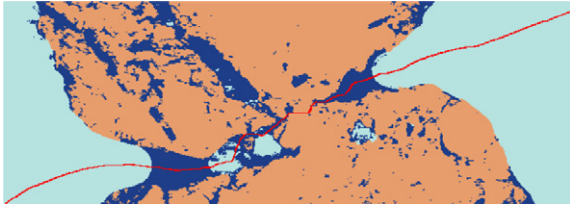


Fig. 13. Vertical cross-section through a detail of two wet soil aggregates touching each other. The image is a segmented X-ray tomogram. The water distribution is visualized with dark blue. The red line indicates the location of the medial surface between the two aggregates. (For interpretation of the references in color in this figure legend, the reader is referred to the web version of this article.)

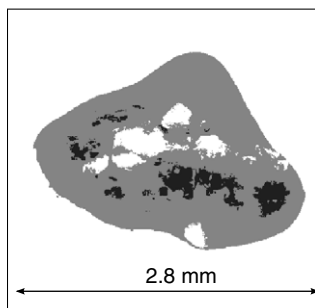


Fig. 14. The three classes air (background), water (gray) and solid (black) mapped on a medial surface.

## 5. Discussion and conclusions

We present two techniques for acquiring images of porous materials, such as soil samples. With our application example, we show how information from the two techniques can be combined to enhance the knowledge of soil transport properties.

Thermal neutrons are optimal for monitoring two-dimensional water distributions during dynamic processes at high temporal resolution. From the recorded water distributions the macroscopic transport properties of the sample can be derived. X-ray images show soil structures and water distributions at much higher resolution in three dimensions. These images contain the relevant information to predict transport properties. By scanning the same or similar samples with the two techniques, macroscopic transport properties of porous media can be linked to the microscopic pore geometry. Indeed, combination of neutron and X-ray techniques offers unique possibilities to improve our knowledge of flow and transport in porous media.

We present two tomographic instruments with different characteristics for acquiring three-dimensional images of soil samples, or more general samples of porous materials. With our application example, we show how the combined information of the two beam modalities can enhance the knowledge required to test hypotheses. Thermal neutrons have the ability to show water distribution within a sample, while X-ray images can show the structures at much higher resolution. Yet, the images alone are not sufficient for a quantitative investigation. Image analysis methods are

required to extract the information from the large amounts of data emerging from the two imaging technologies. The methods of such data analyzes may be already described and applied in other fields, such as in medical applications.

Images alone are not sufficient for a quantitative investigation. Many applications in porous media research are based on the use of bi-level images that describe the porous structure of the investigated samples. Bi-level images are useful for structure quantification and as geometries for simulations, but the water displacement cannot be verified without adding a contrast enhancing component in the fluid. This is the niche where neutron-based imaging has its advantage. By accepting a lower spatial resolution than an X-ray-based system, neutron-based imaging can be used to monitor and quantify three-dimensional water distributions in a sample with much higher accuracy. Recent advances in detector systems and acquisition techniques decrease the beam time required for a tomography. Such technical improvements allow tomography of dynamic processes with a temporal resolution of about 1 min. The ability to monitor water displacement in almost real-time opens many interesting applications in the future. Processing four-dimensional data (three spatial dimensions and time) also requires spatio-temporal image analysis methods. Tasks that will arise are the tracking of a wet front through a heterogeneous sample. For this, methods using active contours and level sets are well suited. For example, Prodanovic et al. [65] used level sets to simulate water movement in a porous medium. By enhancing the image information with a physical model a more precise tracking can be achieved.

There are mainly technical limitations regarding the image-based approach. The major problem is handling the large amounts of data. The problem is two-fold. Firstly, to process images with sizes in the order of  $10^9$  voxels require either computers that can store the entire image in its primary memory (RAM) or methods must be developed that decompose and process the image in smaller regions at the time. The second part of the data-handling problem is storage because a measurement session can easily produce several GB of data. This problem is not so severe but must be considered. Another limitation is the field of view of the scanning system. This limits the sample size for a given resolution. Other limitations are related to the process that is supposed to be observed. The sample must be prepared such that it can be mounted in the scanner. This is especially important for samples that require preconditioning to specific hydraulic conditions. There is a trade-off between ideal process conditions and ideal imaging conditions and the experimental design must account for these limitations.

## Acknowledgements

The authors would like to express their thanks to Hannes Flühler, Andrea Carminati, and Peter Lehmann for their valuable comments and ideas. For the support at the different experiment stations we thank Rene Hassanein,

Peter Vontobel, Felix Beckmann, and Amela Grošo. Finally, without the design and manufacturing of sample containers by Hanspeter Läser these experiments would not have been possible.

## References

- [1] Spanne P, Thovert J, Jacquin C, Lindquist W, Jones K, Adler P. Synchrotron computed microtomography of porous media: topology and transport. *Phys Rev Lett* 1994;73(14):2001–6.
- [2] Duluu OG. Computer axial tomography in geosciences: an overview. *Earth Sci Rev* 1999;48(4):265–81.
- [3] Heijs A, Ritsema C, Dekker L. Three-dimensional visualization of preferential flow patterns in two soils. *Geoderma* 1996;70(2-4):101–16.
- [4] Cislérova M, Votrubová J. CT derived porosity distribution and flow domains. *J Hydrol* 2002;267(3-4):186–200.
- [5] Wildenschild D, Hoppmans J, Vaz C, Rivers M, Rikard D, Christensen B. Using X-ray computed tomography in hydrology: systems, resolutions, and limitations. *J Hydrol* 2002;267(3-4):285–97.
- [6] Lehmann P, Wyss P, Flisch A, Lehmann E, Vontobel P, Krafczyk M, et al. Mapping the structure of porous media using tomography with X-rays from tubes, thermal neutrons and X-rays from synchrotrons: numerical analysis, experiments and applications. *Vadose Zone J* 2006;5(1):80–97.
- [7] Vogel H, Cousin I, Roth K. Quantification of pore structure and gas diffusion as a function of scale. *Eur J Soil Sci* 2002;53:465–73.
- [8] Gibson J, Lin H, Bruns MA. A comparison of fractal analytical methods on 2- and 3-dimensional computed tomographic scans of soil aggregates. *Geoderma* 2006;134(3-4):335–48.
- [9] Yamji A, Yokokawa M, Sao K. Analysis of clustering in three-dimensional grain fabric. *Geosphere* 2007;3(2):108–18.
- [10] Turner M, Knufing L, Arns C, Sakellariou A, Senden T, Sheppard A, et al. Three-dimensional imaging of multiphase flow in porous media. *Physica A* 2004;339:166–72.
- [11] Alshibli K, Sture S, Costes N, Frank M, Lankton M, Batiste S, et al. Assessment of localized deformations in sand using X-ray computed tomography. *Geotech Test J* 2000;23(3):274–99.
- [12] Viggiani G, Lenoir N, Besuelle P, Michiel MD, Marelló S, Desrues J, et al. X-ray microtomography for studying localized deformation in fine-grained geomaterials under triaxial compression. *C R Mech* 2004;332:819–26.
- [13] Prazak J, Tywoniak J, Peterka F, Slonc T. Description of transport of liquid in porous media. a study based on neutron radiography data. *Int J Heat Mass Transfer* 1990;33(6):1105–20.
- [14] Deinert M, Parlange J-Y, Steenhuis T, Throop J, Unlu K, Cady K. Measurement of fluid contents and wetting front profiles by real-time neutron radiography. *J Hydrol* 2004;290(3-4):192–201.
- [15] Abd A-GE, Milczarek J. Neutron radiography study of water absorption in porous building materials: anomalous diffusion analysis. *J Phys D: Appl Phys* 2004;37(16):2305–13.
- [16] Milczarek J, Czachor A, El-Ghany El Abd Z, Wisniewski Abd. Dynamic neutron radiography observations of water migration in porous media. *Nucl Instrum Method Phys Res Sect A: Accel Spectrom Detect Assoc Equip* 2005;542(1-3):232–6.
- [17] Ridgway C, Gane P, Abd A-GE, Czachor A. Water absorption into construction materials: comparison of neutron radiography data with network absorption models. *Transport Porous Media* 2006;63(3):503–25.
- [18] Masschaele B, Dierick M, Hoorebeke LV, Cnudde V, Jacobs P. The use of neutrons and monochromatic X-rays for non-destructive testing in geological materials. *Environ Geol* 2004;46(3-4):486–92.
- [19] Dierick M, Vlassenbroeck J, Masschaele B, Cnudde V, Hoorebeke LV, Hillenbach A. High-speed neutron tomography of dynamic processes. *Nucl Instrum Method Phys Res Sect A: Accel Spectrom Detect Assoc Equip* 2005;542(1-3):296–301.
- [20] Hassanein R, Meyer H, Carminati A, Estermann M, Lehmann E, Vontobel P. Investigation of water imbibition in porous stone by thermal neutron radiography. *J Phys D: Appl Phys* 2006;39(19):4284–91.
- [21] Lehmann E, Frei G, Kühne G, Boillat P. The micro-setup for neutron imaging: a major step forward to improve the spatial resolution. *Nucl Instrum Method Phys Res A* 2007;576:389–96.
- [22] Stapanoni M, Borchert G, Wyss P, Abela R, Patterson B, Hunt S, et al. High resolution X-ray detector for synchrotron-based microtomography. *Nucl Instrum Method Phys Res A* 2002(491):291–301.
- [23] Kak A, Slaney M. Principles of computerized tomographic imaging. IEEE Press; 1988.
- [24] Jain A. Fundamentals of digital image processing. Prentice Hall; 1989.
- [25] Feldkamp L, Davis L, Kress J. Practical cone-beam algorithm. *J Opt Soc Am A* 1984;1(6):612–9.
- [26] Rivers M. Tutorial introduction to X-ray computed microtomography data processing; 1998. <<http://www-fp.mcs.anl.gov/xray-cmt/rivers/tutorial.html>>.
- [27] Raven C. Numerical removal of ring artefacts in microtomography. *Rev Sci Instrum* 1998;69(8):2978–80.
- [28] Sijbers J, Postnov A. Reduction of ring artefacts in high resolution micro-CT reconstructions. *Phys Med Biol* 2004;49:N247–53.
- [29] Jähne B. Digital image processing. 2nd ed. Springer-Verlag; 2002.
- [30] Perona P, Malik J. Scale-space and edge detection using anisotropic diffusion. *IEEE Trans Pattern Anal Mach Intell* 1990;12(7):629–39.
- [31] Catté F, Lions P-L, Morel J-M, Coll T. Image selective smoothing and edge detection by nonlinear diffusion. *SIAM J Numer Anal* 1992;29(1):182–93.
- [32] Osher S, Rudin LI. Feature-oriented image enhancement using shock filters. *SIAM J Numer Anal* 1990;27(4):919–40.
- [33] Aubert G, Kornprobst P. Mathematical problems in image processing. Applied mathematical sciences, vol. 147. Springer-Verlag; 2002.
- [34] Weickert J, ter Haar Romeny B, Viergever M. IEEE transactions on image processing. Efficient Reliable Schemes Nonlinear Diffus Filter 1998;7(3):310–98.
- [35] Kaestner A, Scheebeli M, Graf F. Visualizing three-dimensional rootnext term networks using computed tomography. *Geoderma* 2006;136(1-2):459–69.
- [36] The insight tool kit (ITK). <<http://www.itk.org/>>.
- [37] Sheppard A, Sok R, Averdunk H. Techniques for image enhancement and segmentation of tomographic images of porous materials. *Physica A* 2004;339:145–51.
- [38] Alvarez L, Mazorra L. Signal and image restoration using shock filters and anisotropic diffusion. *SIAM J Numer Anal* 1994;31(2):590–605.
- [39] Thirion J-P, Gourdon A. Computing the differential characteristics of iso-intensity surfaces. *Comput Vis Image Understand* 1995;61(2):190–202.
- [40] Welk M, Weickert J, Galic I. Theoretical foundations for spatially discrete 1D shock filtering. *Image Vis Comput* 2007;25:455–63.
- [41] Rudin L, Osher S, Fatemi E. Nonlinear total variation based noise removal algorithms. *Physica D* 1992;60:259–68.
- [42] Scherzer O, Groetsch C. Inverse scale space theory for inverse problems. *Lect Notes Comput Sci* 2001;2106:317–25.
- [43] Burger M, Gilboa G, Osher S, Xu J. Nonlinear inverse scale space methods. *Commun Math Sci* 2006;4(1):179–212.
- [44] Lie J, Nordbotten J. Inverse scale spaces for nonlinear regularization. *J Math Imaging Vis* 2006;27:41–50.
- [45] Black MJ, Sapiro G, Marimont DH, Heeger D. Robust anisotropic diffusion. *IEEE Trans Image Process* 1998;7(3):421–32.
- [46] Otsu N. A threshold selection method from gray-level histograms. *IEEE Trans Syst Man Cybern* 1979;9(1):62–6.
- [47] Kay S. Fundamentals of statistical signal processing: detection theory, vol. 2. Prentice Hall; 1998.
- [48] Kapur JN, Sahoo PK, Wong AKC. A new method for gray-level picture thresholding using the entropy of the histogram. *Comput Vis Graph Image Process* 1985;29(3):273–85.

- [49] Rosin PL. Unimodal thresholding. *Pattern Recognit* 2001;34(11): 2083–96.
- [50] Adams R, Bischof L. Seeded region growing. *IEEE Trans Pattern Anal Mach Intell* 1994;16(6):641–7.
- [51] Fan J, Zeng G, Body M, Hacid M-S. Seeded region growing: an extensive and comparative study. *Pattern Recognit Lett* 2005;26: 1139–56.
- [52] Soille P. *Morphological image analysis*. 2nd ed. Springer-Verlag; 2002.
- [53] Vogel H, Kretschmar A. Topological characterization of pore space in soil – sample preparation and digital image-processing. *Geoderma* 1996;73(1–2):23–38.
- [54] Ketcham R. Computational methods for quantitative analysis of three-dimensional features in geological specimens. *Geosphere* 2005;1(1):32–41.
- [55] Pierret A, Capowiez Y, Belzunces L, Moran C. 3D reconstruction and quantification of macropores using X-ray computed tomography and image analysis. *Geoderma* 2002;106(3–4):247–71.
- [56] Oh W, Lindquist WB. Image thresholding by indicator kriging. *IEEE Trans Pattern Anal Mach Intell* 1999;21(7):590–602.
- [57] Al-Raoush R, Willson C. A pore-scale investigation of a multiphase porous media system. *J Contam Hydrol* 2005;77:67–89.
- [58] Bigun J. *Vision with direction*. Berlin/Heidelberg: Springer-Verlag; 2006.
- [59] Wildenschild D, Hopmans J, Rivers M, Kent A. Quantitative analysis of flow processes in a sand using synchrotron-based X-ray microtomography. *Vadose Zone* 2005;4:112–26.
- [60] Burt PJ, Hong T-H, Rosenfeld A. Segmentation and estimation of image region properties through cooperative hierarchical computation. *IEEE Trans Syst Man Cybern* 1981;SMC-11(12):802–9.
- [61] Marfil R, Molina-Tanco L, Bandera A, Rodriguez J, Sandoval F. Pyramid segmentation algorithms revisited. *Pattern Recognit* 2006;39:1430–51.
- [62] Videla A, Lin C-L, Miller J. Watershed functions applied to a 3D image segmentation problem for the analysis of packed particle beds. *Particle Particle Syst Charact* 2006;23:237–45.
- [63] Osher S, Paragios N, editors. *Geometric level set methods in imaging, vision, and graphics*. New York: Springer-Verlag; 2003.
- [64] Carminati A, Kaestner A, Hassanein R, Vontobel P, Flühler H. Infiltration through series of soil aggregates. *Adv Water Resour* 2007;30(5):1168–78.
- [65] Prodanovic M, Bryant S. A level set method for determining critical curvatures for drainage and imbibition. *J Colloid Interf Sci* 2006;304: 442–58.